JOURNAL OF CATALYSIS 132, 21–40 (1991)

Deactivation in Catalytic Hydrodemetallation

II. Catalyst Characterization

BARBARA J. SMITH[1] AND JAMES WEI

Department of Chemical Engineering, Massachusetts Institute of Technology, Cambridge, Massachusetts 02139

Received November 2, 1989; revised May 22, 1991

This paper details the characterization of metal-sulfide deposits on catalysts aged in model-compound hydrodemetallation studies. Transmission electron microscopy provides evidence that nickel and vanadium sulfides were present on the catalyst as large and spatially dispersed crystallites. A study of a series of samples with different nickel loadings on a $CoMo/Al_2O_3$ catalyst shows that the diameter of the nickel-sulfide crystallites increased with increasing nickel loading, whereas the number of crystallites per unit volume remained approximately constant. X-ray photoelectron spectroscopy of these samples yielded nickel to aluminum signal ratios significantly lower than the bulk composition. This result is consistent with the nickel-sulfide deposits having a crystallite form, and inconsistent with them being uniform on the catalyst surface. Vanadium-sulfide crystallites on an aged $CoMo/Al_2O_3$ catalyst were similar in size and number-density to nickel-sulfide crystallites on the same catalyst. In contrast, nickel-sulfide crystallites on a low-promoter alumina carrier were significantly larger, and therefore had a smaller number-density, than those on an equivalently loaded $CoMo/Al_2O_3$ catalyst.

1. INTRODUCTION

Detailed characterization of the form of metal-sulfide deposits as a function of metal loading is an important step in identifying the mechanisms by which hydrodemetallation catalysts deactivate, and consequently in designing better catalysts. It is commonly postulated that metal sulfides accumulate in a uniform manner, building up layer by layer and effectively blocking access to the surface of the catalyst after the deposition of just one monolayer-equivalent (*1*). However, the model of locally uniform deposition has not been demonstrated directly by examination of the catalyst surface. In fact, the available evidence suggests that at industrial hydrotreating conditions vanadium is present in crystallite form as V_2S_3 or V_3S_4 (*2–4*).

The objective of this work is to characterize the metal-sulfide deposits on catalysts aged in model-compound hydrodemetallation. Specifically, we address the following questions:

- What is the morphology and distribution of nickel- and vanadium-sulfides deposited on a $CoMo/Al_2O_3$ catalyst?
- How do nickel-sulfide deposits change as the nickel loading is increased from 5 to 100 wt% Ni on a $CoMo/Al_2O_3$ catalyst?
- How do nickel-sulfide deposits on a low-promoter alumina carrier differ from those on a $CoMo/Al_2O_3$ catalyst?

As background for studying the nature of deposited metal sulfides we need to understand the microstructure of hydroprocessing catalysts and the morphology and distribution of the catalytically active phases. Working hydrotreating catalysts are transition-metal sulfides dispersed on a high surface area support, typically alumina. Typical compositions of the catalysts, as received, are 3 to 20 wt% Group VIB metal

[1] Present address: Chevron Research and Technology Company, Richmond, CA 94802.

0021-9517/91 $3.00

oxide and 1 to 8 wt% Group VIII metal oxide (*5*). The catalysts are sulfided before use. At typical loadings, the Group VIB metal sulfides (MoS_2 and WS_2) are present in quantities of less than one monolayer-equivalent. High-resolution electron microscopy indicates that the Mo (or W) is well dispersed on the catalyst surface, as MoS_2-like crystallites. These crystallites lie perpendicular to the surface of the support, in domains or islands of about 3 nm in diameter, and a few layers thick. High-resolution micrographs show lattice fringe spacings of about 0.6 nm for MoS_2 crystallites imaged parallel to the basal plane (*6*). This result is in keeping with the 0.63-nm spacing of the (002) basal planes of MoS_2.

The Group VIII metals (cobalt and nickel) are known to have a promotional effect on catalytic activity. Topsoe and co-workers (*7–9*) have proposed that the catalytically active promoter is present as a "Co–Mo–S" or "Ni–Mo–S" phase. This phase retains the slab-like structure of MoS_2 but has cobalt or nickel associated with it, most likely at the edges and/or corners of the MoS_2 slabs. High-resolution electron microscopic studies have not been able to resolve the nature of the Group VIII promoter (*6*).

Pioneering work on the nature of metal sulfides deposited during catalytic hydrodemetallation was performed by Silbernagel and Riley (*2, 10, 11*). They used nuclear magnetic resonance (NMR) and electron spin resonance (ESR) to trace the deposition of vanadium onto $CoMo/Al_2O_3$ from heavy oil feeds. At low loadings (up to 0.7 wt% vanadium) a vanadyl VO^{2+} species dominated ESR spectral components suggesting that the VO^{2+} ion was associated with defect sites on the alumina support. At higher vanadium loadings a diamagnetic vanadium species was observed by NMR. This phase could have been a sulfide or an oxysulfide; its composition could not be determined by the techniques used. The irregularity of the absorption signal suggested that the vanadium was present in a number of physically different sites, so a vanadium surface species was suspected. The maximum loading of this diamagnetic species was 5–10 wt%, suggesting that it might be present as a monolayer on the catalyst surface. At higher loadings vanadium was present as a sulfide, with composition very close to V_2S_3. Scanning electron microscopy (SEM) analysis suggested that the sulfide was present as crystallites, rather than as a surface phase.

Fleisch *et al.* (*3*) analyzed spent resid demetallation catalysts, containing up to 90 wt% V and Ni, using X-ray photoelectron spectroscopy (XPS) and X-ray diffraction (XRD). The vanadium, nickel, and sulfur XPS spectra were interpreted as metal sulfides, probably V_3S_4 and Ni_3S_2 or Ni_2S. X-ray diffraction confirmed the presence of bulk-like V_3S_4. Takeuchi *et al.* (*12*) used XRD, ESR, and SEM to analyze catalysts used in the hydrotreating of heavy oils. They observed a V_3S_4 phase, in acicular or rod-shaped crystallites about 100 nm in length.

Using high-resolution electron microscopy, Toulhoat *et al.* (*4*) recently observed $Ni(V_3S_4)$ crystallites in a catalyst aged in the hydrodemetallation of deasphalted Boscan crude. Nickel was always associated with vanadium. Crystallite size was observed to increase radially with increasing metal loading. Crystallite sizes ranged from 5 to 30 nm. Typically crystallites grew perpendicularly to the alumina platelets.

Carbonaceous deposits also contribute to the deactivation of hydroprocessing catalysts. This is a complex subject, which has not been well addressed in the literature. However, as discussed in the previous paper in this series (*13*), our catalysts have relatively low deposited carbon loadings (5–7 wt% C) because of the conditions under which they were generated. For this reason the role of carbon in HDM catalyst deactivation is not addressed directly in this paper.

Table 1 summarizes some important properties of the phases found in aged hydroprocessing catalysts.

2. EXPERIMENTAL

We used a variety of techniques to characterize aged catalysts with deposited metal loadings of 6 to 100 wt% Ni and 25 wt% V.

TABLE 1

Bulk Properties of Sulfided Catalyst Phases[a]

Phase	Properties (*14, 15*)		Crystalline habit (*14–17*)
γ-Al_2O_3	MW	101.96	White
	D	3.5–3.9 g/ml	Form similar to cubic spinel $MgAl_2O_4$, with varying degrees of disorder (*18*)
MoS_2	MW	160.07	Black, lustrous
	D	4.80 g/ml	Hexagonal, weak bonding between vicinal sulfur layers a = 3.160 Å, c = 12.294 Å, V = 2 × 53.17 Å^3
Co–Mo–S[b]	Bulk properties unknown		Co located at edges and/or corners of MoS_2 slabs
Co_9S_8[b,c]	MW	786.9	Lustrous
	D	4.6–5.0 g/ml	Isometric a = 10.07 Å, Z = 4
Ni_3S_2	MW	240.19	Pale yellowish bronze color, lustrous
	D	5.82 g/ml	Rhombohedric, close to cubic a = 4.08 Å, α = 90.3°, V = 68.0 Å^3
V_2S_3	MW	198.06	Green-black plates or powder
	D	4.72 g/ml	Monoclinic, sulfur-rich V_3S_4 a = 5.816 Å, b = 3.266 Å, c = 11.310 Å β = 91.50°, V = 214.7 Å^3
$CH_{0.5-1.5}$	D (*19, 20*)	0.8–1.5 g/ml	Amorphous coke

[a] Phases present at reaction conditions.

[b] According to Topsoe (*8*), at the Co and Mo loadings present on sulfided HDS16A the cobalt is divided approximately equally between the Co–Mo–S phase and a Co_9S_8 phase (neglecting a small fraction which is present as the spinel $CoAl_2O_4$).

[c] Properties of the mineral pentlandite $(Fe, Ni, Co)_9S_8$ (*16*).

All the aged-catalyst samples were generated in model compound hydrodemetallation. We used two catalysts: a $CoMo/Al_2O_3$ hydrodesulfurization catalyst (American Cyanamid HDS16A; 8.1 wt% Mo, 4.5 wt% Co), and an alumina substrate with low levels of Co, Ni, and Mo promoters on it (American Cyanamid HDS3 substrate; 0.24 wt% Mo, 0.68 wt% Co, 0.32 wt% Ni). The details of these catalysts and the experiments in which they were aged are reported by Smith and Wei (*13*).

Table 2 presents a summary of all the catalyst samples, and the analyses performed on them. Almost all samples were characterized for pore-size distribution (nitrogen desorption), surface area (nitrogen adsorption), and elemental composition (atomic absorption spectroscopy and microcombustion). In addition, selected catalyst samples were analyzed using electron microprobe analysis (Cameca Microbeam), transmission electron microscopy (TEM, JEOL 120CX), scanning transmission electron microscopy (STEM, VG HB5 with TRACOR energy dispersive X-ray analyzer), X-ray photoelectron spectroscopy (PHI 548), and X-ray diffraction (Siemens D501).

Samples were prepared for TEM and STEM using an ultramicrotoming procedure developed at the Institut Français du Pétrole. Catalyst particles were embedded in low viscosity resin (Polarbed 812, Polaron Instruments Inc., Hatfield, PA) that was then polymerized at 60°C for 48 h. A three-step procedure was used to prepare thin sections of the sample for TEM. First, a clean razor blade was used to cut a regular and level trapeze from the resin surrounding the sample. Ultramicrotoming was accomplished with a glass knife, to thicknesses of 150 nm, then with a diamond knife, to final sample thicknesses in the range 60–80 nm. Samples were collected on carbon-coated copper grid.

XPS samples were prepared by dusting

TABLE 2

Catalyst Characterization Summary

Sample	Metal[a] (wt%)	Carbon[a] (wt%)	Solvent	SA (m^2/g)	EMPA	XRD	TEM	STEM	XPS
				Catalysts					
$CoMo/Al_2O_3$ (HDS16A)	—	—	—	176	○	√	○	○	√
SA00 (sulfided HDS16A)	—	5.1	Kaydol	150[b]	○	○	√	○	√
Low-promoter alumina carrier (HDS3 substrate)	—	—	—	258	○	○	√	○	○
				Nickel deposited on $CoMo/Al_2O_3$					
SA08	22.9	6.9	Kaydol	98[b]	√	○	○	○	√
SA09	6.1	6.9	Kaydol	100[b]	√	○	√	√	○
SA10	37.1	7.2	Kaydol	99[b]	√	○	√	○	○
SA11	27.3	4.2	Squalane	100[b]	√	○	○	○	○
SA12	70.8	5.2	Squalane	45[b]	√	√	√	√	√
SA15[c]	12.0	○	Squalane	○	√	○	○	√	○
SA18	(100)[d]	○	Squalane	○	√	○	√	○	○
				Vanadium deposited on $CoMo/Al_2O_3$					
SA17	25.4	4.9	Squalane	78[b]	√	√	√	√	○
				Nickel deposited on low-promoter alumina carrier					
AL13	22.5	2.5	Squalane	○	√	○	√	○	○

Note. Key: √, measured; ○, not measured; — not relevant. Techniques: SA, surface area. EMPA, electron microprobe analysis. XRD, X-ray diffraction. TEM, transmission electron microscopy. STEM, scanning transmission electron microscopy. XPS, X-ray photoelectron spectroscopy.

[a] Ni or V, fresh catalyst basis.

[b] Measured using BET one-point method.

[c] 300-μm particles.

[d] Calculated by mass balance.

the catalyst powder on sticky copper tape. Some outgassing was generally observed when the sample was introduced to the ultrahigh vacuum chamber. XPS signals were collected from a 3 × 3-mm region, using Mg$K\alpha$ X-ray as the excitation source. No electron flood gun was used in this work, and depth profiling of the samples by sputtering was not attempted.

3. BULK ANALYSIS RESULTS

Elemental Compositions

The metal (nickel or vanadium) and carbon analyses of the aged-catalyst samples are summarized in Table 2. All compositions are reported on a fresh catalyst basis. These calculations were done by normalizing with the aluminum compositions of the fresh catalysts, which are 41.9 wt% for the $CoMo/Al_2O_3$ catalyst, HDS16A, and 51.7 wt% for the low-promoter alumina carrier, HDS3 substrate. The nickel and vanadium analyses agree with expected results calculated by mass balance from solution concentrations in the hydrodemetallation experiments. In some cases the deposited nickel loadings have been increased beyond the end-of-run values reported in Smith and Wei

(*13*), by carrying out additional Ni-etioporphyrin (Ni-EP) HDM experiments.

The carbon loadings on the aged-catalyst samples were consistently about 5 wt% for the catalysts aged in squalane, and about 7 wt% for those aged in Kaydol. These results confirm the low coking tendency of these solvents at the relatively low temperatures used for these experiments. The slightly higher level of carbon deposited with Kaydol as a solvent is consistent with a greater coking tendency of the naphthenic and aromatic components of Kaydol, relative to paraffinic squalane. The invariance in the levels of deposited carbon suggests that an equilibrium coke level was established on the catalyst very rapidly, and this level did not change substantially as metal-sulfide deposits accumulated.

Surface Area

Table 2 summarizes surface area measurements. We used the single-point BET method for the aged-catalyst samples, and the accuracy of these results is limited by the small quantities of sample available for analysis. The results show an expected decline in surface area as metal-sulfide deposits accumulate. We observed an initial sharp decline in surface area from 150 m^2/g (sulfided catalyst, SA00) to 100 m^2/g (several catalysts in the range 5–35 wt% Ni). A substantial portion of this loss can be attributed to coking. At higher metal loadings greater surface area losses were observed. At 25 wt% V (SA17) the surface area had declined to about 80 m^2/g. At 70 wt% Ni (SA12) it had declined to 45 m^2/g.

X-Ray Diffraction

X-ray diffraction analysis was made of samples SA12 (70 wt% Ni on $CoMo/Al_2O_3$) and SA17 (25 wt% V on $CoMo/Al_2O_3$). The XRD spectra are given by Smith (*21*). The XRD spectrum for SA12 showed clear evidence for a bulk Ni_3S_2 phase. Some properties of Ni_3S_2 are summarized in Table 1. The XRD spectrum of SA17 was less conclusive because the vanadium loading was relatively low. The spectrum is consistent with the presence of vanadium as V_2S_3, or possibly V_5S_8. V_2S_3 is a sulfur-rich form of V_3S_4. Since previous characterization of spent HDM catalysts has indicated that bulk vanadium is present as V_2S_3 or V_3S_4 (*2, 3, 4*), for estimating properties of the deposited phase we assume that the bulk vanadium phase on our catalysts is V_2S_3. The properties of bulk V_2S_3 are summarized in Table 1.

4. HIGH-RESOLUTION ELECTRON MICROSCOPY

In all our high-resolution microscopy studies, we took care to ensure that the micrographs represented the catalyst samples accurately. All samples were examined thoroughly at low magnification for any inhomogeneities. In addition, many catalyst particles and many regions of each particle were examined for each sample.

For most of the samples, the radial metal deposition profiles across the catalyst particles were flat (see the electron microprobe analyses reported in Smith and Wei (*13*)). Thus, no systematic variation in metal composition as a function of radial position was expected. Our treatment of the two samples, which did exhibit deposited-metal gradients, SA15 and SA17, is discussed in more detail below.

One important point about interpretation of the micrographs should be noted. The thickness of the TEM and STEM catalyst samples is approximately 70 nm, significantly greater than the characteristic dimension of the alumina platelets and the deposit crystallites. For this reason these features overlap in the micrographs. The pores of catalyst substrate are not imaged directly.

4.1. Nickel on $CoMo/Al_2O_3$

Comparison of nickel on $CoMo/Al_2O_3$ samples. Figure 1 shows TEM micrographs, all at the same magnification, of four catalyst samples: SA00, SA10, SA12, and SA18. Micrograph 1a shows sample SA00, a sulfided $CoMo/Al_2O_3$ catalyst that has not been subjected to hydrodemetallation. Micrographs 1b, 1c, and 1d show catalysts that were aged

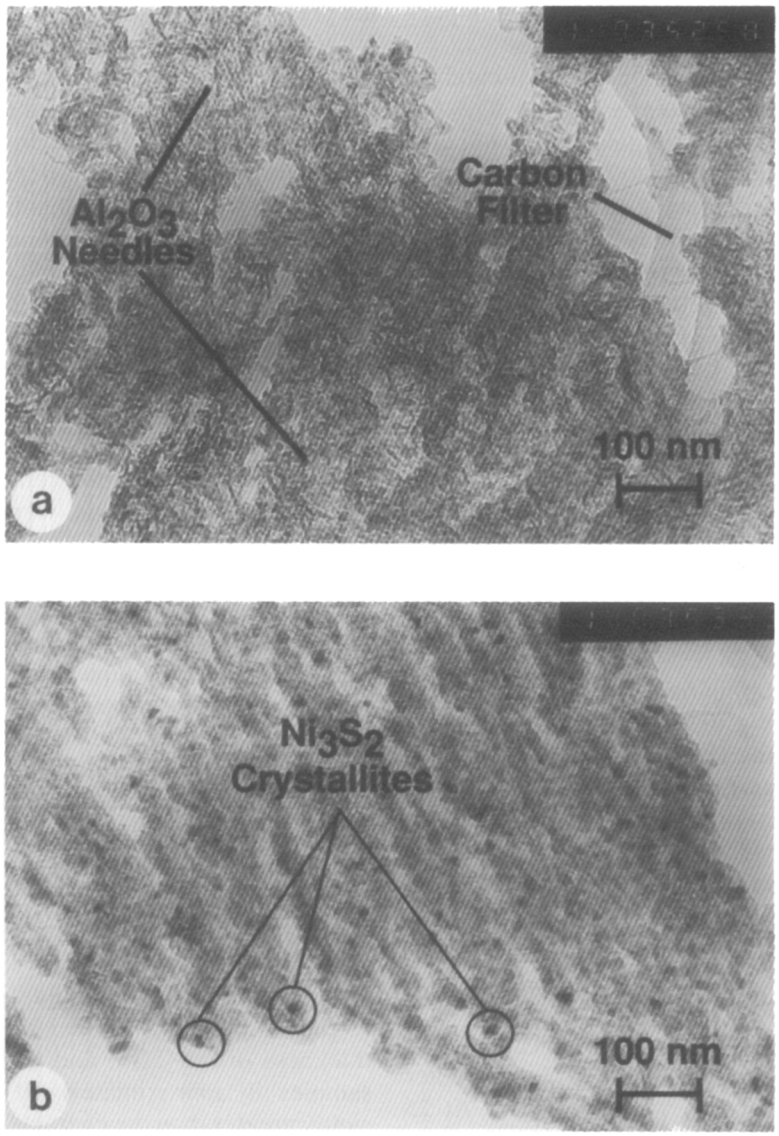

FIG. 1. TEM micrographs, all at the same magnification of four catalyst samples with various levels of deposited nickel on $CoMo/Al_2O_3$. (a) SA00 (0 wt% Ni); (b) SA10 (37 wt% Ni); (c) SA12 (70 wt% Ni); (d) SA18 (100 wt% Ni).

by Ni-EP hydrodemetallation to deposited nickel loadings of about 37 wt%, 70 wt%, and 100 wt%.

For best resolution, Fig. 1a shows a region in which most of the sample is over a hole in the carbon film of the TEM support. The boundary of the carbon film can be seen on the right-hand side of the micrograph. The sample is of varying thickness. The voids in the micrograph are regions where sample was lost in microtoming; they do not correspond to catalyst porosity. The dominant features of this micrograph are the alumina platelets that comprise the catalyst substrate. These platelets are needle-like, approximately 3 nm (30 Å) in diameter and 25 nm (250 Å) in length.

Comparison of Figs. 1b, 1c, and 1d with

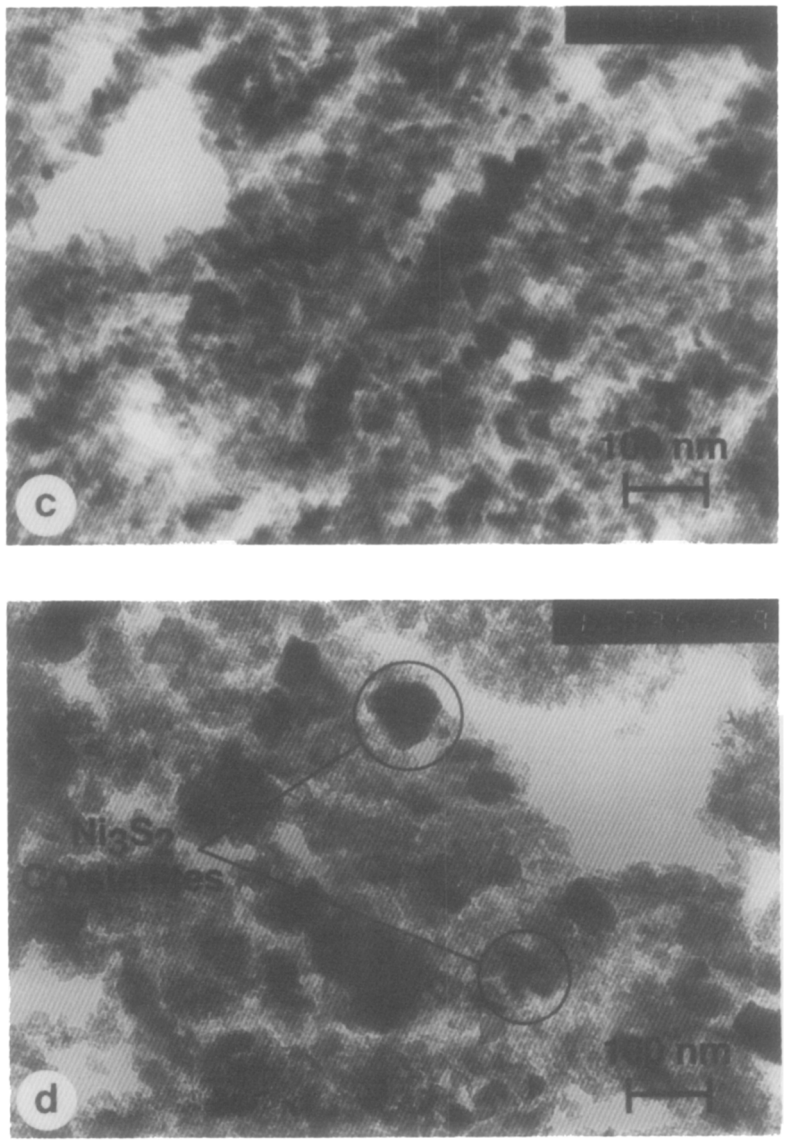

FIG. 1—*Continued*

Fig. 1a shows that deposited nickel introduced a new feature to the TEM micrographs: spatially dispersed nickel-sulfide crystallites. Because of overlap, the thick, dark regions in the micrographs are not necessarily single crystallites. Nevertheless, it is apparent that increased metal loading corresponds to increased crystallite size.

We quantified the changes in the size and number densities of the nickel-sulfide crystallites in the aged-catalyst samples to obtain a better understanding of the growth process. This kind of quantification also allowed us to estimate the nickel loading on the catalysts, and check the correspondence between microscopic and bulk analyses.

Confirmation of nickel phase. Figure 2 is a higher-magnification micrograph of catalyst sample SA10. It shows several MoS_2 fringes, in stacks of two or three layers. The spacing between lattice fringes is close to

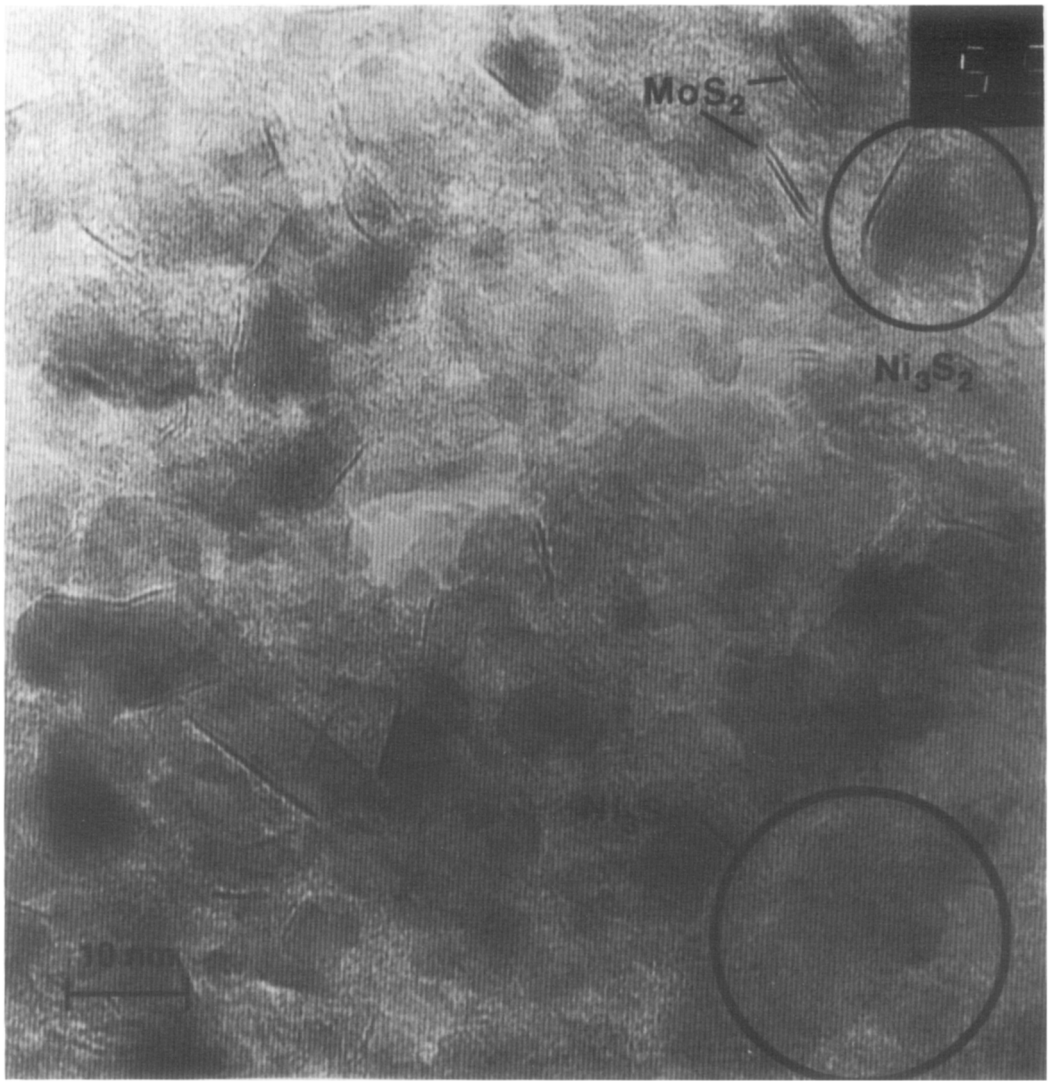

FIG. 2. TEM micrograph of sample SA10 (37 wt% nickel on $CoMo/Al_2O_3$) at higher magnification.

the 0.6 nm expected for MoS_2 (*6*). Figure 2 also shows many Ni_3S_2 crystallites that are randomly oriented and in many cases overlapping. The spacing of their lattice fringes is noticeably smaller than those for MoS_2. It is consistent with the 0.4 nm expected for Ni_3S_2, the nickel-sulfide phase detected by X-ray diffraction.

We confirmed the Ni_3S_2 phase assignment with STEM/EDX analysis of aged-catalyst samples. Details of this work are given by Smith (*21*). In summary, STEM analysis of a very thin region of sample SA12 allowed us to image isolated deposit crystallites. Many of the crystallites had a regular shape, apparently close to the rhombohedral morphology of Ni_3S_2. EDX microanalysis of eight such crystallites gave sulfur to nickel ratios consistent with the stoichiometry of Ni_3S_2. We made a sulfur mass balance by accounting for the sulfur associated with nickel, molybdenum, and cobalt as Ni_3S_2,

MoS_2, and CoS. It closed to within 10%, the accuracy limit of this technique.

Crystallite size as a function of metal loading. We used a standard method for sizing and counting crystallites in most of the samples. To minimize misinterpretations caused by the overlap of two or more crystallites, we used high-magnification micrographs such as Fig. 2 (sample SA10), in which the lattice fringes of the crystallites are visible. We counted only crystallites for which lattice fringes are visible, and we estimated the mean crystallite diameter by averaging over all such crystallites. Using this method, we estimated the characteristic diameter of the crystallites to be 9.5 nm in sample SA10, 12 nm in SA12, and 15 nm in SA18.

We estimated crystallite size for Sample SA09 (6 wt% Ni) from both TEM and STEM micrographs. (See the micrographs in Smith (*21*).) Our best estimate of mean crystallite size was 5 nm. We note, however, that even high-magnification images of this sample show very few deposit crystallites.

Sample SA15, with a mean catalyst-particle diameter of 300 μm, had been aged under mildly diffusion-limited HDM conditions. Electron microprobe analysis, reported in Smith and Wei (*13*), confirmed that the catalyst particles had the expected U-shaped nickel deposition profile. It was highest at the outer edge of the catalyst particles (about 11 wt% Ni) and declined monotonically toward the center (about 9 wt% Ni). We estimated crystallite size directly from the STEM micrographs for this sample. (See the micrographs in Smith (*21*). No lattice fringe images were available because this sample was not examined with TEM.) The observed nickel-sulfide crystallite size did not vary significantly across the particle radius, because of the relatively small variation in nickel loading. Consequently, we report just the mean value of 6 nm.

Number of crystallites per unit volume. We counted the number of crystallites showing lattice fringes carefully for two of the nickel-aged samples, SA10 and SA12, and then used two additional parameters to quantify the number of crystallites per unit volume. The first parameter, sample thickness, was estimated as 70 nm, the approximate thickness achieved by ultramicrotoming. This multiplied by the area of the micrograph gave the sample volume. The second parameter was the fraction of the total number of crystallites for which lattice fringes were visible. This was estimated as 0.05, by assuming that lattice fringes were imaged only if the orientation of the crystal plane was close enough to the direction of the electron beam that adjacent planes did not appear to overlap (0.4-nm lattice fringe spacing/8-nm crystallite dimension). Using these two parameters, the number of crystallites per unit volume was estimated as 5×10^{-4} nm^{-3} for sample SA10 and 4×10^{-4} nm^{-3} for SA12.

The number of crystallites imaged was too small for a good count with samples SA09 and SA15. No estimate of the number of crystallites per unit volume was made for sample SA18, because the large, thick-deposit crystallites and the extensive overlap between crystallites made accurate counting difficult to count.

Nickel mass balance. We calculated a total nickel loading for samples SA10 and SA12, for which we had estimates of both mean crystallite size and the number of crystallites per unit volume. Table 3 summarizes these calculations. We assumed spherical crystallites. The nickel loadings calculated by mass balance were 60 wt% Ni for SA10 and 104 wt% Ni for SA12; 150 and 165%, respectively, of the measured bulk catalyst compositions. Given the uncertainty in the parameters used to estimate the number of crystallites per unit volume this represents acceptable agreement.

For the catalyst samples analyzed by STEM we compared local EDX analyses with the bulk atomic-absorption analyses. These results further confirmed the correspondence between micro-scale and macro-scale observations of catalyst composition. For sample SA09 the mean EDX nickel

TABLE 3

Summary of TEM Observations—Crystallite Size and Distribution

Nominal metal loading (wt%)	Sample	Mean crystallite diameter (nm)	Crystallites per unit volume (nm^{-3})	Mass balance[a]
		Nickel on $CoMo/Al_2O_3$		
6	SA09	5	—	<100%
10	SA15	6	—	<100%
37	SA10	9.5	5×10^{-4}	165%
70	SA12	12	4×10^{-4}	150%
100	SA18	15	—	—
		Vanadium on $CoMo/Al_2O_3$		
25	SA17	8	6×10^{-4}	105%
		Nickel on low-promoter alumina carrier		
22	AL13	25	5×10^{-6}	55%

[a] Mass balance is the ratio of metal loading estimated from TEM observations, assuming spherical metal sulfide crystallites, to the nominal metal loading for the sample as reported in Table 2.

loading was 3 wt% Ni (average for five regions), somewhat lower than the bulk composition of 6 wt% Ni. For sample SA15 the mean EDX nickel loading was 12 wt% Ni (average for six regions), close to the bulk composition of 10 wt% Ni. Because of the uncertainty of EDX microanalysis (±10%) and the relatively shallow metal deposition profile in this sample, we did not see any significant variation in the nickel loadings as we looked across the catalyst particle.

The growth of Ni_3S_2 crystallites with increasing nickel loading. Figure 3 shows mean crystallite diameter plotted as a function of deposited nickel loading on the $CoMo/Al_2O_3$ catalyst. The solid curve is the predicted diameter, assuming spherical crystallites and 3×10^{-4}-nm^{-3} crystallites per unit volume. This simple model for spherical crystallites fits the TEM observations very well. Thus the TEM results are consistent with a nucleation and growth model in which the number of nucleation sites remained constant, and the size of the crystallites increased as the deposited nickel loading increased. The following paper (*22*) develops this concept further. It extends the crystallite growth model and allows for overlap effects between neighboring crystallites.

Do Ni_3S_2 deposits grow on MoS_2 crystallites? We made a rough estimate for the number density of MoS_2 crystallites in the $CoMo/Al_2O_3$ catalyst by using catalyst properties (particle density = 1.49 g/ml, Mo loading = 8.1 wt%), and MoS_2 crystallite dimensions consistent with XPS and TEM observations. We assumed MoS_2 crystallites 6 nm across and an average of three layers high, with a density of 4.6 g/ml. These values yield an estimate for the number density of MoS_2 crystallites of 8×10^{-4} nm^{-3}. This is of the same order as the number density of nickel-sulfide crystallites estimated from the HREM studies, 3×10^{-4} nm^{-3}, and is thus suggestive of a correspondence between MoS_2 crystallites and the nucleation sites for nickel-sulfide crystallites.

We examined the micrographs carefully for any evidence of correspondence between the locations of nickel-sulfide deposits and the MoS_2 crystallites. Some high-magnification TEM images of Ni_3S_2 crystallites, including the one in the upper right of Fig. 2, do show a single dark fringe reminiscent of MoS_2 at one edge of the Ni_3S_2

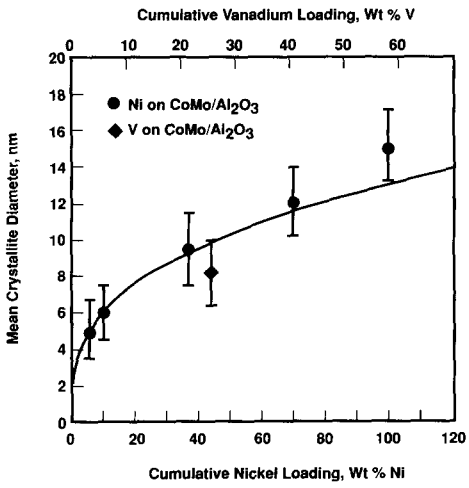

FIG. 3. Mean crystallite diameter, as measured by TEM, versus cumulative metal loading. Solid curve is predicted crystallite diameter, assuming spherical crystallites, 3×10^{-4} nm^{-3} crystallites per unit volume, and no overlap between crystallites.

lattice fringes. However, close examination of a number of these crystallites using STEM/EDX did not give any consistent evidence for high molybdenum concentrations at these edges. Thus, we have no conclusive evidence from this study for a correspondence between the locations of nickel-sulfide deposits and the MoS_2 crystallites.

4.2 *Vanadium on* $CoMo/Al_2O_3$

Sample description. We used TEM and STEM to examine one sample (SA17) that had vanadium-sulfide deposits on the $CoMo/Al_2O_3$ catalyst. Because this sample was aged under diffusion-limited conditions the vanadium was deposited in the catalyst particles with a radial concentration-gradient. Electron microprobe analysis, reported in Smith and Wei (*12*), confirmed that the vanadium concentration was highest and the particle exterior (about 28 wt% V) and declined monotonically toward the center (about 18 wt% V). However, this variation is relatively small and, according to the trends seen with the series of nickel-aged catalysts, not sufficient to cause significant variations in crystallite size or distribution. For this reason we did not systematically examine variations in this sample across the catalyst-particle radius. Rather, we averaged observations made at random positions within the particles.

Figure 4a shows a TEM micrograph of sample SA17. The alumina platelets that comprise the $CoMo/Al_2O_3$ catalyst are evident throughout the micrograph. Comparison with Fig. 1a, a micrograph of sulfided catalyst that had not been subjected to hydrodemetallation, shows that, as in the case of nickel-sulfide deposits, the presence of vanadium sulfide introduced a new feature, dark spots confirmed by further analysis to be spatially dispersed vanadium-sulfide crystallites. Figure 4b shows a higher magnification view of the same catalyst sample. A number of MoS_2 fringes are apparent, in stacks of two, three, and four layers. The spacing between lattice fringes is close to the value of 0.6 nm expected for MoS_2. Many V_2S_3 crystallites, which are randomly oriented and in some cases overlapping, are also evident.

Confirmation of the vanadium phase. Figure 5 shows a STEM micrograph of the sample SA17. It shows an isolated crystallite of which we made a high-resolution microanalysis. Figure 6 shows EDX spectra for this crystallite and for a larger region of about 400 × 600 nm, which incorporated the area shown in Fig. 5. The crystallite analysis gave very low aluminum and molybdenum signals, and a vanadium to sulfur ratio within 10% of the stoichiometric ratio for V_2S_3, the vanadium-sulfide phase indicated by X-ray diffraction. This confirmed that the crystallites are V_2S_3.

Size and number density of the V_2S_3 *crystallites.* We used the same methods for sizing and counting V_2S_3 crystallites as for most of the nickel-aged samples (SA10, SA12, SA18). The mean diameter of the crystallites in Fig. 4b was estimated as 8 nm, by averaging over all crystallites for which lattice fringes are visible.

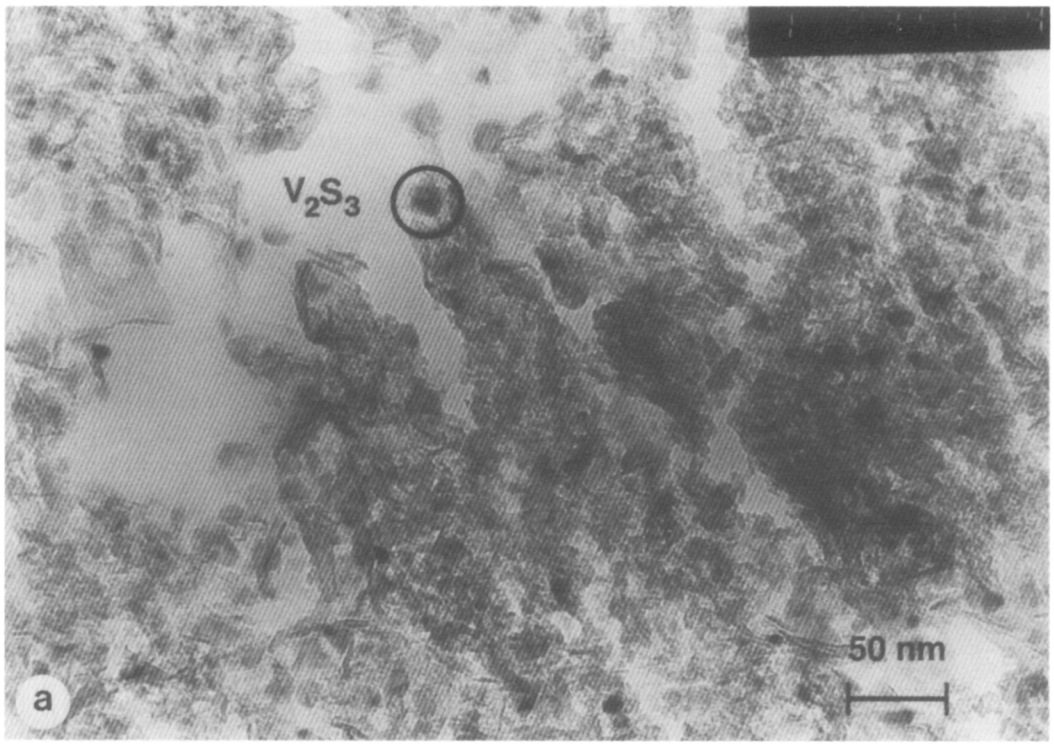

FIG. 4. TEM micrographs, at two magnifications, of sample SA17 (25 wt% vanadium on $CoMo/Al_2O_3$).

The mean crystallite diameter for this vanadium case is plotted as a diamond on Fig. 3, along with the nickel observations. Note that the cumulative vanadium and nickel x-axis scales have been adjusted to correspond to equivalent volumes of metal-sulfide deposits. Within the uncertainty bounds of estimating crystalite size from TEM micrographs, the vanadium result follows the trend in crystallite diameter as a function of metal loading observed for nickel deposits.

The number of crystallites per unit volume for sample SA17 was estimated as 6×10^{-4} nm^{-3} from Fig. 4b. As shown in Table 3, this value is very close to the results for nickel-aged catalysts SA10 and SA12.

Vanadium mass balance. We calculated a total vanadium loading for sample SA17 by assuming spherical crystallites with the mean dimension of 8 nm. As shown in Table 3, the result was 26 wt% V, or 105% of the measured catalyst composition. Given the uncertainty in the parameters used to estimate the number of crystallites per unit volume this represents an acceptable mass balance.

The EDX global analysis shown in Fig. 6 indicated a vanadium to aluminum ratio within 15% of the bulk atomic-absorption analysis for this catalyst. This further confirmed the correspondence between microscale and macroscale observations of catalyst properties.

4.3. Nickel on Low-Promoter Al_2O_3 Carrier

Sample descriptions. Figure 7 shows a TEM micrograph of a sample of the low-promoter alumina carrier (HDS3 substrate), which we used for these comparative studies. The sample shown had not been sulfided or subjected to hydrodemetallation. The dominant features of this micrograph are the alumina platelets that comprise the sub-

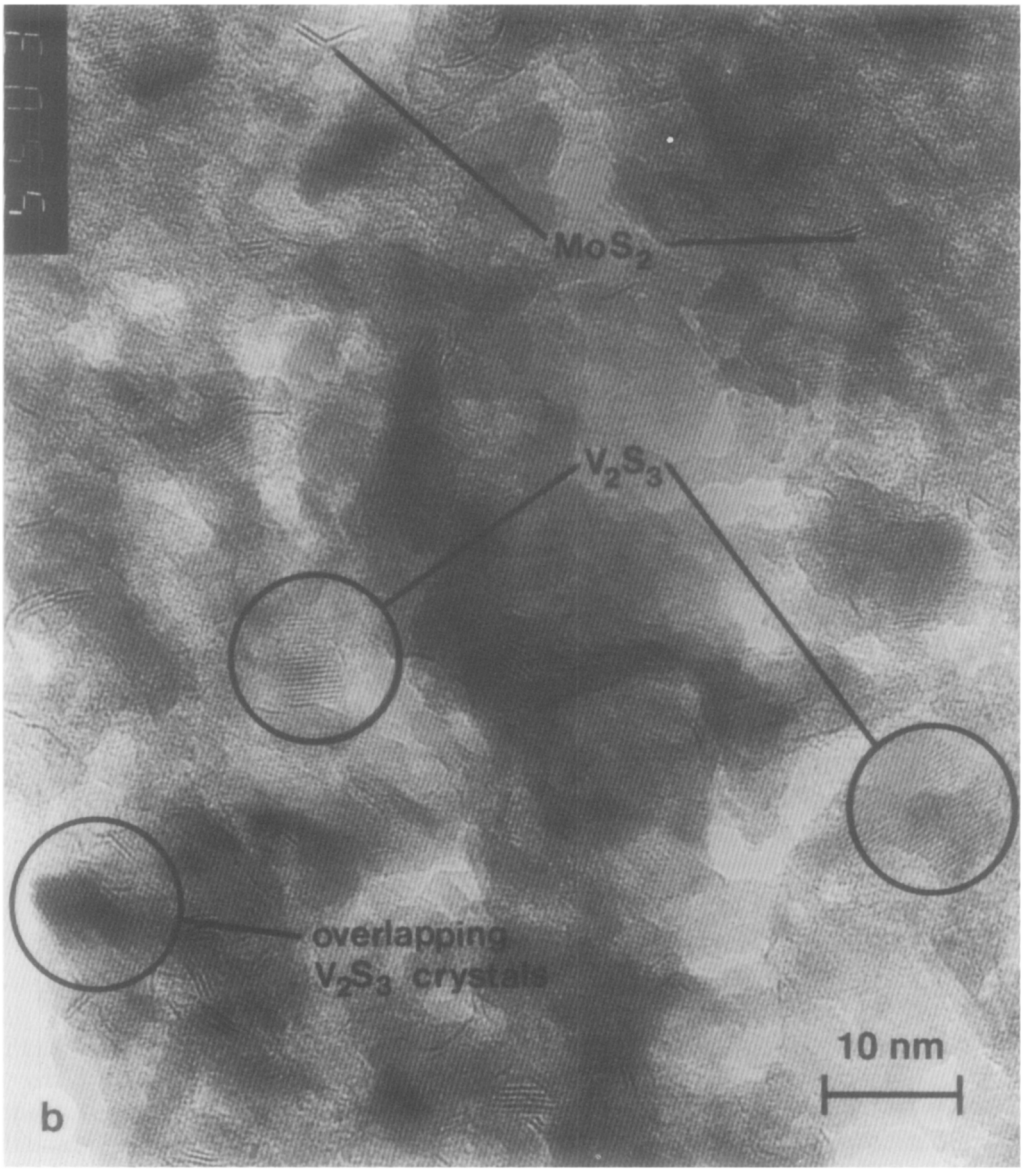

FIG. 4—*Continued*

strate. These platelets are needle-like, with diameters of approximately 3 nm (30 Å) and lengths up to 50 nm (500 Å).

Figure 8 shows a TEM micrograph of sample AL13, the low-promoter alumina carrier, loaded to about 25 wt% nickel in Ni-EP hydrodemetallation. Comparison of Figs. 7 and 8, which are at the same magnification, shows clearly the spatially dispersed Ni_3S_2 crystallites in the aged sample.

Size and number density of the Ni_3S_2 crystallites. The characteristic dimension of the crystallites in Fig. 8 was estimated as 25 nm by averaging over all the visible crystallites. (For this sample the crystallites were large and distinct enough that direct counting of

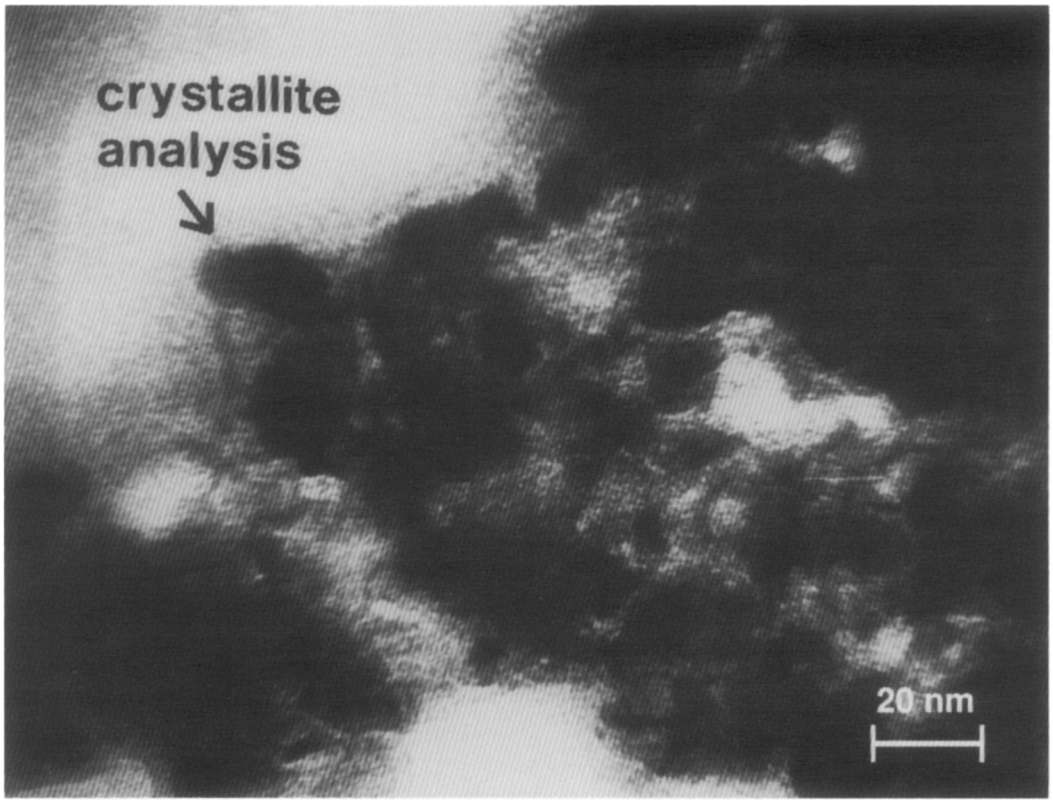

FIG. 5. STEM micrograph of sample SA17 (25 wt% vanadium on $CoMo/Al_2O_3$) showing a particle used for EDX crystallite analysis.

the crystallites, rather than averaging over those crystallites for which lattice fringes were visible only, was used as a counting method.) The number of crystallites per unit volume was estimated as 5×10^{-6} nm^{-3} from the micrographs, assuming a sample thickness of 70 nm as previously.

Nickel mass balance. With the assumption of spherical crystallites, a nickel mass balance was made using the estimates for the mean crystallite dimension and the number of crystallites per unit volume. The calculated nickel loading was 12 wt% Ni, or about 55% of the measured bulk catalyst composition. Some crystallites were probably not counted due to overlap. Thus, given the uncertainty in the estimated value of the number of crystallites per unit volume, this represents an acceptable mass balance.

Comparison of deposits on the $CoMo/Al_2O_3$ catalyst and the low-promoter alumina carrier. Comparison of Fig. 8 with Fig. 1b shows a clear difference in the size of deposited crystallites for similarly loaded samples of the $CoMo/Al_2O_3$ catalyst and the low-promoter alumina carrier. Table 3 summarizes the TEM observations of crystallite size and dispersion for all samples. It shows that the mean crystallite size observed on the low-promoter alumina carrier was significantly larger than that for all the observations of metal-sulfide crystallites on the $CoMo/Al_2O_3$ catalyst. Consequently, the number of crystallites per unit volume in the alumina carrier was lower than that in the $CoMo/Al_2O_3$.

In fact, the number of crystallites per unit volume that closed the nickel mass balance

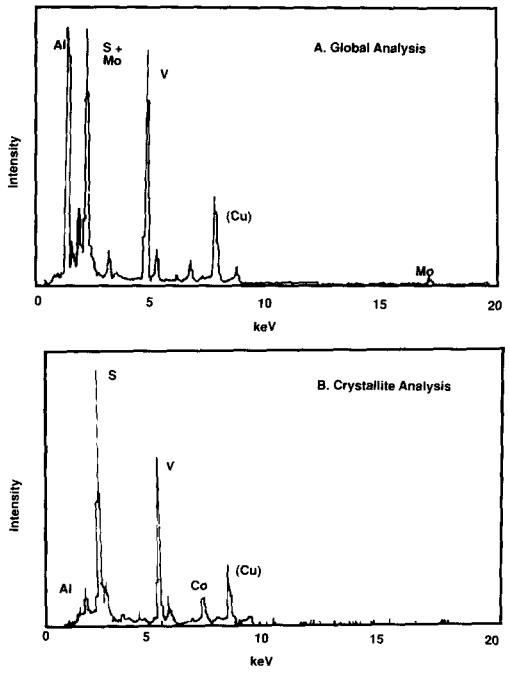

FIG. 6. EDX micro-analysis spectra. (a) Global analysis of a region of about 400 × 600 nm, which incorporated the area shown in Fig. 5. (b) Crystallite analysis of the particle identified in Fig. 5.

for the alumina carrier, assuming 25 nm spherical crystallites, was about 1×10^{-5} nm^{-3}. This was about 3% of the number of crystallites per unit volume found for the $CoMo/Al_2O_3$ catalyst. We note from Table 4 that this proportion is close to the relative concentrations of promoters in the two catalysts. This suggests a direct correspondence between promoter loadings and the density of crystallite nucleation sites. Because of the limited nature of the study of the alumina carrier, this finding cannot be taken as conclusive. However, we believe that it warrants further investigation.

5. X-RAY PHOTOELECTRON SPECTROSCOPY

X-ray photoelectron spectroscopy has been used extensively to characterize the $CoMo/Al_2O_3$ catalyst system. Most of this work has addressed the chemical state of the molybdenum and cobalt on the catalysts, as a function of loading and pretreatment conditions. Briggs and Seah (*23*) present a summary of this work. However, microporous catalysts present a number of problems for quantification by XPS. In particular, binding-energy shifts and peak broadening caused by charging effects can make chemical state assignments uncertain. For these reasons we did not attempt to elucidate chemical state information using XPS.

The main application of XPS in this work was to assess the dispersion of nickel-sulfide deposits on aged catalysts. We measured XPS intensities for several samples of the $CoMo/Al_2O_3$ catalyst that had been aged in Ni-EP HDM. Then we compared experimental results with predictions for electron-flux attenuation from three different quantitative models. Our models were based on the work of Kerkhof and Moulijn (*24*) and Kuipers *et al.* (*25*). The simplest was a homogeneous-mixture model. The other two were based on a simple-sheet model of the catalyst (*24*). They assumed an alumina-sheet thickness of 6.5 nm, based on the void fraction and surface area properties of the catalyst. In the uniform-deposits model we assumed that nickel sulfide deposited in a uniform layer on both sides of the alumina sheet, and the thickness of the deposit layer increased as the metal loading increased. In the crystallite-deposits model we assumed cubic crystallites of the dimensions observed by TEM (15 nm at 100 wt% nickel) on both sides of the alumina sheet.

The models all assumed that electrons leave the sample only in a direction perpendicular to the surface and that flux is attenuated exponentially with distance through the solid. The inelastic mean free path, λ, was used to characterize the attenuation of electron flux. The values of the electron mean free paths inside the catalyst matrix are not known very precisely. A value of 2.5 nm was used for λ_{Al}, based on the work of Defosse (*26*). A value of 0.6 nm was estimated for λ_{Ni}, based on correlations given by Briggs and Seah (*23*).

Figure 9 shows Ni/Al XPS intensity ratios as a function of cumulative nickel loading

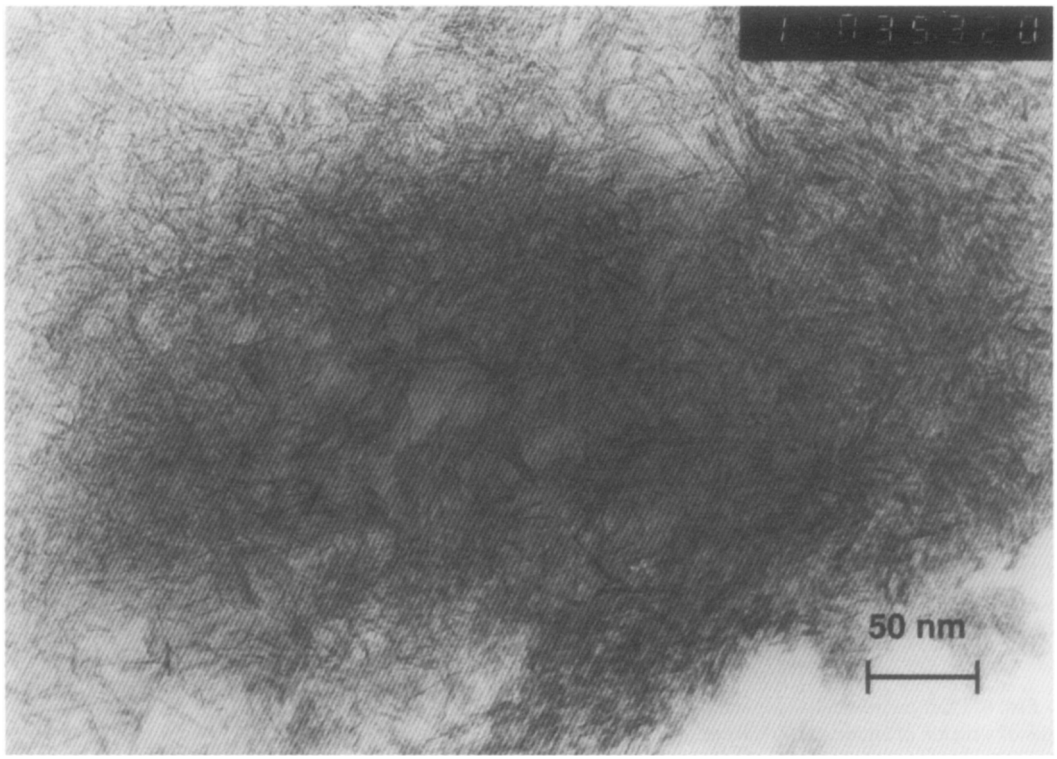

FIG. 7. TEM micrograph of the low-promoter alumina carrier.

for a number of catalyst samples, and solid lines representing the three different models for the dispersion of the deposited nickel-sulfide phase. The measured nickel to aluminum signal ratios were significantly lower than expected for either a homogeneous-mixture model (assuming the bulk composition) or a uniform-deposits model. The Ni/Al intensity ratio from the uniform-deposits model was even higher than that corresponding to a homogeneous-mixture because the photoelectron mean free path of Ni 2*p* is considerably shorter than that of Al 2*p*.

The prediction from a simple crystallite-deposits model, which assumed cubic crystallites of the dimensions observed by TEM, was much closer to the experimental observations. This model yielded a much lower Ni/Al intensity ratio because in this case only a small volume of the "surface" nickel was sampled by XPS. The discrepancy between the crystallite-deposits model and the measured intensity ratios may be partially explained by the presence of a contamination overlayer. The Ni/Al signal ratio would be diminished by any contamination because the electron mean free path for nickel is less than that for aluminum.

These simple models neglected orientation effects, and the electron mean free paths and atomic sensitivity factors used were only approximate values. Nevertheless, they do indicate that our XPS results were consistent with our high-resolution electron microscopy observations of a crystallite form for nickel-sulfide deposits.

6. DISCUSSION

The crystallite dimensions found in this study for metal-sulfide deposits on the $CoMo/Al_2O_3$ catalyst correspond with those reported by Toulhoat *et al.* (*4*) for $(Ni)V_3S_4$ crystallites on a $NiMo/Al_2O_3$ catalyst used

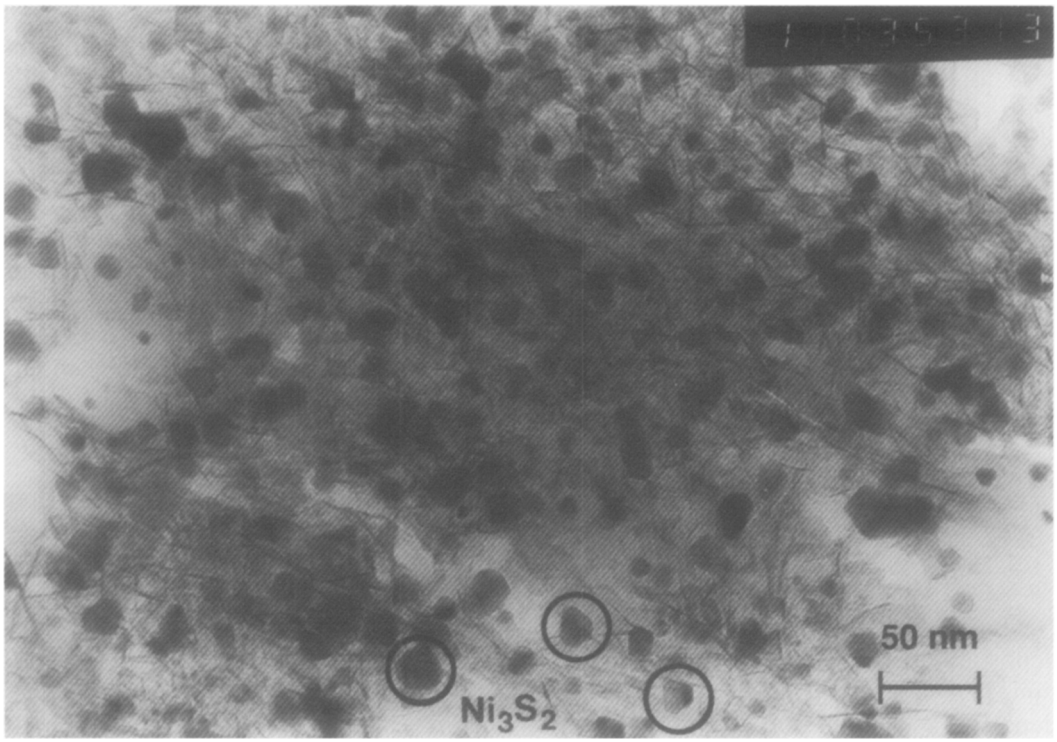

FIG. 8. TEM micrograph of sample AL13 (25 wt% nickel on a low-promoter alumina carrier).

in the hydrodemetallation of deasphalted Boscan crude. The catalyst used by Toulhoat *et al.* had promoter loadings somewhat lower than the $CoMo/Al_2O_3$ catalyst used in these studies (4.7 wt% Mo, 1.2 wt% Ni). The catalyst was aged under diffusion-limited conditions. In experiments conducted at 400°C, the crystallite dimension ranged from 30 nm at the particle exterior, where the metal loading was 115 wt% (Ni + V), to 5 nm at the particle center, where the metal loading was about 20 wt% (Ni + V). This similarity between catalysts aged in model compound HDM and catalysts aged with petroleum feedstock is encouraging. It suggests that the catalysts aged in the porphyrin HDM experiments provide a useful representation of catalysts aged with petroleum feeds. And it suggests that our conclusions on crystallite size and number density, which are based on a series of samples aged under conditions that produce flat metal deposition profiles across the catalyst particle radius, can be applied to the case of catalysts aged under diffusion-limited conditions that have deposited metal gradients.

Silbernagel and Riley (*10, 11*), who used

TABLE 4

Comparison of the Low-Promoter Alumina Carrier and the $CoMo/Al_2O_3$ Catalyst

	Concentration in the alumina carrier relative to the $CoMo/Al_2O_3$ catalyst
Promoters	
Molybdenum	2%
Total promoter (Ni + Co + Mo)	7%
Phosphorous	4%
Number of crystallites per unit volume	3%

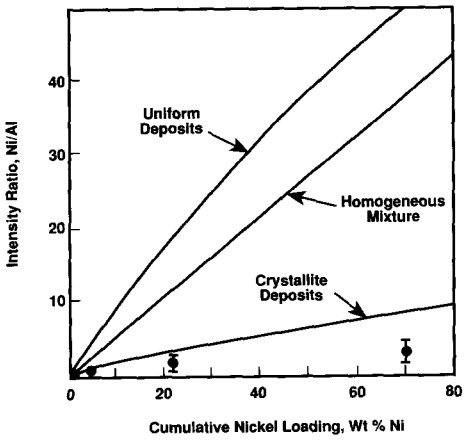

FIG. 9. X-ray Photoelectron Spectroscopy Ni/Al intensity-ratio versus cumulative nickel loading on the $CoMo/Al_2O_3$ catalyst.

NMR and ESR to study vanadium sulfides deposited during catalytic hydrodemetallation, postulated that the first 5–10 wt% of deposited vanadium formed a surface species. In our catalysts, a monolayer of deposited metal sulfides on the catalyst surface is equivalent to approximately 30 wt% Ni or 15 wt% V (calculations summarized in (*21*)). On the basis of the available evidence it is not possible to eliminate the possibility that a small fraction of the deposited metal is present as a surface layer. The mass balance errors inherent in TEM and STEM are large enough that these techniques do not allow us to conclude that all deposited metal is in the crystallite form. And although our XPS results (Fig. 9) are inconsistent with a uniform-layer model for nickel deposition, we have insufficient data on catalysts with low deposit loadings to conclude that the first fraction of a monolayer-equivalent is not present as a uniform layer on the catalyst surface.

7. CONCLUSIONS

This paper details the characterization of metal-sulfide deposits on catalysts aged in model-compound hydrodemetallation. Our conclusions are as follows:

(1) High-resolution electron microscopy (TEM and STEM) shows that nickel and vanadium sulfides were deposited in the catalysts in the form of large and spatially dispersed crystallites. The crystallites were generally regular in shape.

(2) Microcombustion analysis of the catalyst samples confirmed that coke loadings were relatively low, 5 wt% for the samples aged in squalane and 7 wt% for the samples aged in Kaydol. Coke deposits could not be detected in any of the TEM or STEM studies. No difference in the metal-sulfide crystallite morphology or dispersion was apparent for the samples aged in the two solvents.

(3) At high metal loadings the deposited crystallites were larger than the measured pore diameters of the catalysts. The $CoMo/Al_2O_3$ catalyst had a pore diameter of 8 nm. In it we observed Ni_3S_2 crystallites as large as 15 nm (at 100 wt% Ni) and V_2S_3 crystallites of 8-nm diameter (at 25 catalyst% V). The low-promoter alumina carrier had a pore diameter of 8 nm. In it we observed Ni_3S_2 crystallites of 25 nm (at 22 wt% Ni). These observations are consistent with a model of the catalyst as an agglomeration of alumina platelets, and the catalyst pore space as the void between these fine particles. A deposit crystallite nucleates on the surface of a catalyst particle and grows to fill the surrounding void, encompassing nearby catalyst particles if necessary. In the following paper we develop a quantitative model for the growth of metal-sulfide crystallites in porous catalysts. The model is based directly on our HREM observations of the two catalysts studied here, but is simplified in that the needle-like alumina platelets and the metal-sulfide crystallites are modeled as spheres. The model is used to predict changes in catalyst properties as deposits accumulate.

(4) For the $CoMo/Al_2O_3$ catalyst, we observed that the diameter of the nickel- and vanadium-sulfide crystallites increased monotonically with increasing nickel loading. Conversely, the number density of crystallites remained approximately constant.

(Note, however, that this observation was made over a relatively limited range of metal loadings.) We showed that this result is consistent with a simple model for the growth of crystallites, in which the number of metal-sulfide crystallites remains constant and the size of the crystallites increases with increasing deposited metal loading.

(5) We made direct counts of crystallite number density for three of the aged $CoMo/Al_2O_3$ catalysts, and found values ranging from 4 to 6 $\times$ 10^{-4} nm^{-3}. In addition, our simple model of crystallite growth used a value of in 3 $\times$ 10^{-4} nm^{-3} for the number density of deposited crystallites in the $CoMo/Al_2O_3$ catalyst. These estimates are of the same order as the number density of MoS_2 crystallites, 8 $\times$ 10^{-4} nm^{-3}, suggesting a correspondence between MoS_2 crystallites and nucleation sites for nickel-sulfide crystallites. There was no direct evidence for such a conclusion, however. With the inherent uncertainties in interpreting high-resolution electron microscopy images, we conclude that no correspondence was observable between the metal-sulfide crystallites and MoS_2 crystallites on the catalyst.

(6) TEM examination of the low-promoter alumina carrier showed differences between the deposits on it and those on the $CoMo/Al_2O_3$ catalyst. It had relatively larger nickel-sulfide crystallites, and a smaller number of crystallites per unit volume. In fact, the TEM results for the two catalysts were consistent with a direct correspondence between promoter loading and density of crystallite nucleation sites. The loadings of cobalt, nickel, molybdenum, and phosphorous promoters on the alumina carrier relative to the catalyst were approximately proportional to the number of crystallites per unit volume in the two catalysts. We consider these results suggestive, but not conclusive.

(7) We estimated metal loadings on the aged catalysts from the TEM observations of crystallite size and number density. These estimates agreed with measurements made using atomic absorption spectroscopy within a factor of two. This suggests good correspondence between microscopic and bulk analyses of the aged catalyst.

(8) X-ray photoelectron spectroscopy of a series of $CoMo/Al_2O_3$ catalysts at different nickel loadings yielded nickel to aluminum signal ratios significantly lower than those predicted for a homogeneous mixture at the bulk composition. This result is consistent with a crystallite-deposits model for nickel sulfide, but inconsistent with a uniform-layer model. Thus indirect spectroscopic evidence (XPS) confirms the direct microscopic evidence (TEM and STEM) that nickel and vanadium sulfides deposit on HDM catalysts in the form of relatively large and spatially dispersed crystallites.

APPENDIX: NOMENCLATURE

EDX	Energy dispersive X-ray analysis
EMPA	Electron microprobe analysis
HREM	High resolution electron microscopy
Ni-EP	Nickel etioporphyrin
PV	Pore volume
SA	Surface area
STEM	Scanning transmission electron microscopy
TEM	Transmission electron microscopy
XPS	X-ray photoelectron spectroscopy
XRD	X-ray diffraction
λ	Electron inelastic mean free path

ACKNOWLEDGMENTS

The authors are grateful to Dr. H. Toulhoat, Dr. R. Szymanski, and the members of the electron microscopy team at the Institut Français du Pétrole in Reuil-Malmaison, France. All the high-resolution electron microscopy work reported in this paper was carried out at IFP. The authors also acknowledge the assistance of John Martin and Libby Shaw of the MIT Central Surface Analytical Facility with the XPS work.

REFERENCES

1. Tamm, P. W., Harnsberger, H. F., and Bridge, A. G., *Ind. Eng. Chem. Process Des. Dev.* **20,** 262 (1981).

2. Silbernagel, B. G., *J. Catal.* **56,** 315 (1979).
3. Fleisch, T. H., Meyers, B. L., Hall, J. B., and Ott G. L., *J. Catal.* **86,** 147 (1984).
4. Toulhoat, H., Plumail, J. C., Houpert, C., Szymanski, R., Bourseau, P., and Muratet, G., *in* "ACS Div. Petrol. Chem., Symposium on Advances in Resid Upgrading, Denver, April 1987."
5. Quann, R. J., Ware, R. A., Hung, C. H., and Wei, J., *Adv. Chem. Eng.* **14,** 95 (1988).
6. Delannay, F., *Appl. Catal.* **16,** 135 (1985).
7. Topsoe, H., *NATO ASI Ser. C* **105,** 329 (1983).
8. Topsoe, H., and Clausen, B. S., *Catal. Rev. Sci. Eng.* **26,** (3–4), 395 (1984).
9. Topsoe, H., Candia, R., Topsoe, N. Y., and Clausen, B. S., *Bull. Soc. Chim. Belg.* **93** (8–9), 783 (1984).
10. Deleted in proof.
11. Silbernagel, B. G., and Riley, K. L., *in* "Catalyst Deactivation" (B. Delmon and G. F. Froment, Eds.), Vol. 6, p. 313. Elsevier, Amsterdam, 1980.
12. Takeuchi, C., Asoka, S., Nakata, S., and Shiroto, Y., *ACS Prepr. Div. Petrol. Chem.* **30** (1), 96 (1985).
13. Smith, B. J., and Wei, J., *J. Catal.* **132,** 1 (1991).
14. Weast, R. C., "Handbook of Chemistry and Physics." CRC Press, Cleveland, 1982.
15. Hurlbut, C. S., and Klein, C., "Manual of Mineralogy." Wiley, New York, 1979.
16. Weisser, O. A., and Landa, S., "Sulfide Catalysts, Their Properties and Applications." Pergammon, Oxford, 1973.
17. de Vries, A. B., and Jellinek, F., *Rev. Chim. Miner.* **11,** 624 (1974).
18. Satterfield, C. N., "Heterogeneous Catalysis in Practice." McGraw–Hill, New York, 1980.
19. Beuther, H., and Schmid, B. K., *Proc. 6th World Petrol. Congr.* Sect. III, Paper 20 (1963).
20. Scaroni, A. W., Jenkins, R. G., and Walker, P. L., *Appl. Catal.* **14,** 173 (1985).
21. Smith, B. J., Sc.D. thesis, Massachusetts Institute of Technology, 1988.
22. Smith, B. J., and Wei, J., *J. Catal.* **132,** 41 (1991).
23. Briggs, D., and Seah, M. P., "Practical Surface Analysis." Wiley, New York, 1979.
24. Kerkhof, F. P. J. M., and Moulijn, J. A., *J. Phys. Chem.* **83,** 1612 (1979).
25. Kuipers, H. P. C. E., van Leuven, H. C. E., and Visser, W. M., *Surf. Interface Anal.* **8,** 235 (1986).
26. Defosse, C., *J. Electron Spectrosc. Relat. Phenom.* **23,** 157 (1981).